

Asymmetry and condition number of an elliptic-parabolic system for biological network formation

Clarissa Astuto¹, Daniele Boffi^{1,2}, Jan Haskovec¹, Peter Markowich^{1,3}, and Giovanni Russo⁴

¹King Abdullah University of Science and Technology (KAUST), 4700, Thuwal, Saudi Arabia

²Department of Mathematics "F. Casorati", University of Pavia, Pavia, Italy

³Department of Mathematics, University of Vienna, Vienna, Austria

⁴Department of Mathematics and Computer Science, University of Catania, Catania, Italy

January 31, 2023

Abstract

We present results of numerical simulations of the tensor-valued elliptic-parabolic PDE model for biological network formation. The numerical method is based on a non-linear finite difference scheme on a uniform Cartesian grid in a 2D domain. The focus is on the impact of different discretization methods and choices of regularization parameters on the symmetry of the numerical solution. In particular, we show that using the symmetric alternating-direction implicit (ADI) method for time discretization helps preserve the symmetry of the solution, compared to the (nonsymmetric) ADI method. Moreover, we study the effect of regularization by isotropic background permeability $r > 0$, showing that increased condition number of the elliptic problem due to decreasing value of r leads to loss of symmetry. Finally, we perform numerical error analysis of our method in Wasserstein distance.

1 Introduction

Principles of formation, adaptation and functioning of biological transportation networks have been a long standing topic of scientific investigation. It has significant applications in leaf venation in plants [1], vascular pattern formation [2], mammalian circulatory systems or neural networks that transport electric charge [3, 4]. Typical subjects of investigation are geometrical and topological properties of optimal networks, their statistical properties and robustness with respect to damage or varying external conditions. For instance, in mammalian circulatory systems one aim of study is the relation between the dilation of arteries and an augmentation of blood flow [5]. Other studies reveal that local gradient

of pressure can interfere with the diameter of blood vessels as an adaptive response to the stress [6, 7, 8, 9].

In plant leafs, the pattern of their venation seems to influence the cells that are engaged in photosynthesis, and other functionalities of the plant, such as its longevity and the optimal water distribution. Modeling of formation and adaptation of leaf venation is a very challenging task because of the nature of the problem. Every leaf of the same plant exhibits different venation patterns [10]. This is reflected by the inherent non-uniqueness of solutions and, even, instabilities in the corresponding mathematical models. Consequently, it is difficult to validate results of numerical simulations versus experimental observations. A small change in the parameters of the model or its discretization (such as the resolution of the numerical grid) can lead to very different solutions.

The modeling framework for biological network formation introduced by Hu and Cai in [10, 11] involves a purely local dynamic adaptation model based on mechanical laws, consisting of a system of ordinary differential equations (ODE) on graph edges coupled to a linear system of equations for the material pressure. The biological nature of the model is reflected by a metabolic cost function that is proportional to a power of the conductance of the edge. Local conservation of mass is imposed by the Kirchhoff law. The model responds to merely local information and naturally incorporates fluctuations in flow distributions. In [11] a related PDE-based continuum model was proposed, which consists of a parabolic reaction-diffusion equation for the vector-valued network conductivity, coupled to a Poisson equation for the pressure. The model was subsequently studied in the series of papers [12, 13, 14, 15, 16]. A more general model with tensor-valued conductivity was derived in [17]. The two modeling approaches were compared numerically in [18].

This paper focuses on numerical treatment of the tensor-valued PDE model of [17], where the permeability tensor appearing in the Poisson equation is regularized by adding a multiple $r\mathbb{I}$ of the identity matrix, with $r > 0$. We discretize the system in space using a finite-difference scheme on a two-dimensional Cartesian grid. The time discretization is carried out using the alternating-direction implicit (ADI) and symmetric-ADI schemes. The time discretization is crucial since the system is stiff in all its components. The stiffness may lead to loss of symmetry of the solution in situations when all parameters, initial and boundary data are symmetric. The main goal of the paper is to investigate the loss of symmetry and its dependence on the model parameters, in particular on the value of the regularization parameter r . Moreover, we carry out convergence analysis of the method. Here we argue that the Wasserstein distance [19, 20, 21] is an appropriate choice of distance in the convergence analysis. In particular, it is more suitable than the usual L^p -norms to compute the discretization error.

The paper is organized as follows: In Section 2 we introduce the tensor-valued PDE model. In Section 3 we describe the finite-difference semi-implicit schemes that we use for its discretization. In Section 4 we provide the results of the numerical simulations, with focus on investigation of the symmetry of the solution and its dependence on the time discretization

and the parameter values. Finally, in Section 5 we summarize the results and draw some conclusions.

2 The PDE Model

The PDE model [17] consists of an elliptic equation for the pressure $p = p(t, \vec{x}) \in \mathbb{R}$ representing the Darcy's law, and a parabolic reaction-diffusion equation for the tensor-valued conductivity $\mathbb{C} = \mathbb{C}(t, \vec{x})$,

$$-\nabla \cdot ((r\mathbb{I} + \mathbb{C}\nabla p) = S, \quad (1)$$

$$\frac{\partial \mathbb{C}}{\partial t} - D^2 \Delta \mathbb{C} - c^2 \nabla p \otimes \nabla p + \alpha |\mathbb{C}|^{\gamma-2} \mathbb{C} = 0. \quad (2)$$

The term $S = S(\vec{x})$ denotes the distribution of sources and sinks, which has to be prescribed as a datum. The function $r : \Omega \rightarrow \mathbb{R}^+$, with $r(x) \geq r_0 > 0$, describes the isotropic background permeability of the medium. In (2) the diffusion coefficient $D > 0$ controls the random effects in the transportation medium and the activation parameter $c^2 > 0$ describes the tendency of the network to align with the pressure gradient. The reaction term $\alpha |\mathbb{C}|^{\gamma-2} \mathbb{C}$ models the metabolic cost of maintaining the network structure, with metabolic coefficient $\alpha > 0$ and metabolic exponent $\gamma > 0$. For blood circulatory systems we choose $\gamma = 1/2$, see [9] for details, while for modeling of leaf venation in plants we have $1/2 \leq \gamma \leq 1$, see [10, 11].

We pose (1)–(2) on a bounded domain $\Omega \subset \mathbb{R}^2$ with smooth boundary $\partial\Omega$. We choose homogeneous Neumann boundary conditions for \mathbb{C} and p on $\partial\Omega$,

$$\nabla \mathbb{C}(t, \vec{x}) \cdot \nu = 0, \quad \nabla p(t, \vec{x}) \cdot \nu = 0, \quad \vec{x} \in \partial\Omega, \quad t \geq 0 \quad (3)$$

where ν is the outer normal vector to $\partial\Omega$ and the boundary condition for \mathbb{C} is interpreted elementwise, i.e., $\nabla \mathbb{C}_{ij}(t, \vec{x}) \cdot \nu = 0$ for all $i, j = 1, \dots, d$. With the homogeneous Neumann boundary condition for the pressure p , we impose the global mass balance

$$\int_{\Omega} S(\vec{x}) d\vec{x} = 0 \quad (4)$$

to ensure solvability of (1).

Finally, we prescribe a positive semidefinite initial condition $\mathbb{C}^0 \geq 0$ for the conductivity \mathbb{C} ,

$$\mathbb{C}(t = 0, \vec{x}) = \mathbb{C}^0(\vec{x}) \quad \text{in } \Omega. \quad (5)$$

A fundamental observation about the system (1)–(2) is that it represents an L^2 -gradient flow of the energy

$$\mathcal{E}[\mathbb{C}] = \int_{\Omega} \frac{D^2}{2} |\nabla \mathbb{C}|^2 + c^2 \nabla p[\mathbb{C}] \cdot (r\mathbb{I} + \mathbb{C}) \nabla p[\mathbb{C}] + \frac{\alpha}{\gamma} |\mathbb{C}|^{\gamma} d\vec{x},$$

where $p[\mathbb{C}]$ is the unique (up to an additive constant) solution of (1) subject to the homogeneous Neumann boundary condition. In [17] it has been shown that for $\gamma > 1$ the energy functional is coercive and strictly convex. Consequently, it possesses a unique minimizer that describes the optimal transportation structure for the given distribution of sources and sinks S . On the other hand, for $0 < \gamma < 1$ the metabolic term renders the energy highly non-convex with a multitude of critical points. This fact is manifested in the numerical simulations carried out in this paper, where we shall observe their strong sensitivity with respect to the choice of the initial datum \mathbb{C}^0 .

3 Numerical schemes

In this section we briefly describe a fully second order space and time discretization that we adopt in our numerical simulations. We refer to [18] for further details.

3.1 Space discretization

For the discretization in space we choose the two-dimensional quadratic domain $\Omega = [0, 1] \times [0, 1]$ where we construct a uniform Cartesian mesh with spatial step $h := \Delta x = \Delta y$. We denote Ω_h the discrete computational domain. The discretized conductivity, $\mathbb{C}_{ij} \approx \mathbb{C}(x_i, y_j)$, and pressure, $p_{ij} \approx p(x_i, y_j)$, are defined at the center of the cell (i, j) , therefore we have $x_i = (i - 1/2)h$, $y_j = (j - 1/2)h$, $(i, j) \in \{1, \dots, N\}^2$, $hN = 1$. We choose a cell centered discretization because it simplifies the implementation of the homogeneous Neumann boundary condition and guarantees the exact conservation of total mass of the solution.

The space discretization of Eq. (2) written in compact form (see [18] for more details) reads

$$\frac{\partial \mathbb{C}_{\text{comp}}}{\partial t} = D^2 \mathcal{L} \mathbb{C}_{\text{comp}} + c^2 \mathcal{P} - \alpha \mathcal{Q}(\mathbb{C}) \mathbb{C}_{\text{comp}} \quad (6)$$

where \mathcal{L} is the discrete Laplacian operator and \mathcal{D}_x and, resp., \mathcal{D}_y are the discrete first-order derivative operators in the x - and, resp., y -directions. We use the central difference approximation. $\mathbb{C}_{\text{comp}} = [C^{(1,1)}, C^{(1,2)}, C^{(2,2)}]^T$ is the vector of the unknowns for the conductivity, and \mathcal{P} is the matrix of pressure gradients $\mathcal{P} = [\mathcal{D}_x p \mathcal{D}_x p, \mathcal{D}_x p \mathcal{D}_y p, \mathcal{D}_y p \mathcal{D}_y p]$. For the metabolic terms, we have

$$\mathcal{Q}(\mathbb{C}) = |\mathbb{C}|^{\gamma-2}. \quad (7)$$

where $|\cdot|$ denotes the Frobenius norm.

The discretized version of the Poisson equation (1) reads

$$\partial_x \left(\left(r + C^{(1,1)} \right) \partial_x p \right) + \partial_x \left(C^{(1,2)} \partial_y p \right) + \partial_y \left(C^{(1,2)} \partial_x p \right) + \partial_y \left(\left(r + C^{(2,2)} \right) \partial_y p \right) = -S \quad (8)$$

where we use the symmetry of the conductance tensor $C^{(1,2)} = C^{(2,1)}$. We discretize the components of the above formula one by one, since we use different discretizations for each. For simplicity of notation we define $\mathcal{C}^{(1,1)} = r + C^{(1,1)}$ and $\mathcal{C}^{(2,2)} = r + C^{(2,2)}$. Then we have

$$\partial_x \left(\mathcal{C}^{(1,1)} \partial_x p \right)_{i,j} \approx \frac{1}{2\Delta x^2} \left(\left(\mathcal{C}_{i+1,j}^{(1,1)} + \mathcal{C}_{i,j}^{(1,1)} \right) p_{i+1,j} + \left(\mathcal{C}_{i-1,j}^{(1,1)} + \mathcal{C}_{i,j}^{(1,1)} \right) p_{i-1,j} - \left(\mathcal{C}_{i+1,j}^{(1,1)} + \mathcal{C}_{i-1,j}^{(1,1)} + 2\mathcal{C}_{i,j}^{(1,1)} \right) p_{i,j} \right)$$

We omit the term with both y -derivatives because it is analogous to the one with x -derivatives. The term with mixed derivatives is discretized as follows,

$$\begin{aligned} \partial_x \left(C^{(1,2)} \partial_y p \right)_{i,j} &\approx \frac{1}{8\Delta x^2} \left(C_{i+1,j}^{(1,2)} + C_{i,j}^{(1,2)} \right) (p_{i+1,j+1} - p_{i+1,j-1}) \\ &\quad - \frac{1}{8\Delta x^2} \left(\left(C_{i-1,j}^{(1,2)} + C_{i,j}^{(1,2)} \right) (p_{i-1,j+1} - p_{i-1,j-1}) + \left(C_{i+1,j}^{(1,2)} - C_{i-1,j}^{(1,2)} \right) (p_{i,j+1} - p_{i,j-1}) \right) \end{aligned}$$

and analogously for the term with the y, x -derivatives.

3.2 Time discretization: *symmetric*-ADI method and extrapolation technique

In this section we describe the time discretization that we apply to the model. It is a crucial point since the Eq. (2) is very stiff in all its components.

We choose the *symmetric* alternating-direction implicit (ADI) scheme. From its definition, the classical ADI scheme [?] is not symmetric since we choose which direction considering implicit for the first half step and then the second one is automatically chosen. A symmetrized version of this method will compute the average of the two choices.

Another improvement we can make to the ADI method can be found in [22]. We extrapolate the solution of the reaction-diffusion equation to compute the solution of the Poisson equation for the pressure: Given the conductivity tensor at time t^n and t^{n-1} , we extrapolate the conductivity at time $t^{n+1/2}$

$$\mathbb{C}^{n+1/2} = \frac{3}{2}\mathbb{C}^n - \frac{1}{2}\mathbb{C}^{n-1}, \quad (9)$$

then compute $p^{n+1/2}$ by solving the Poisson equation

$$-\nabla \cdot \left(\left(\mathbb{C}^{n+1/2} \right) \nabla p^{n+1/2} \right) = S,$$

which in the discretized version reads

$$-\mathcal{L} \left(\mathbb{C}^{n+1/2} \right) p^{n+1/2} = S. \quad (10)$$

Finally, we apply the *symmetric*-ADI method to solve (6).

In practise we apply twice the traditional ADI scheme. The first time we start with the y -direction implicit in the first step, and, with the x -direction implicit in the second one.

The second time, we exchange the order for the implicit (and automatically also for the explicit) steps. At the end, we calculate the average of the two computed solutions. A numerical comparison between the classical ADI [?] and the symmetric ADI methods is presented in Table 1 below.

3.2.1 Comparisons between ADI and *symmetric*-ADI method

In this section we compare the two versions of the ADI method to see the improvements in the symmetric version. We adopt a symmetric numerical scheme, and we choose symmetric initial datum and source function S . Consequently, the exact solution to the problem retains symmetry at each time step.

In order to check if our scheme is symmetric, we calculate the asymmetry of the solution with the following formula

$$\text{asymm}(A) = \frac{||A - A^T||}{||A + A^T||} \quad (11)$$

In Table 1 we see the comparison between the two ADI schemes, for different choices of the regularization parameter r , representing the background permeability in the elliptic equation (1).

Table 1: *In this table we see the difference between a traditional ADI scheme and the symmetric version, for different values of the background permeability r . The choice of the parameters, the source function S and the initial datum are defined in Eqs. (12-16).*

| | $r = 10^{-2}$ | | $r = 10^{-3}$ | | $r = 10^{-4}$ | |
|-----------------------|---------------|-----------|---------------|-----------|---------------|-----------|
| | ADI | sym-ADI | ADI | sym-ADI | ADI | sym-ADI |
| asymm(\mathbb{C}) | 6.107e-04 | 4.390e-08 | 2.591e-02 | 1.673e-03 | 1.536e-01 | 1.868e-01 |
| asymm(p) | 3.8862e-05 | 4.289e-09 | 6.137e-02 | 2.688e-03 | 2.683e-02 | 2.808e-02 |

Moreover, investigating the reasons why we lose the symmetry of the solution, we notice that it is related to the computation of the solution of the Poisson equation (1) and in the choice of the background permeability r . When this parameters tends to zero, the condition number of the iteration matrix \mathcal{L} increases, up to the order 10^8 . In Fig. 1 we show the quantity defined in Eq. (11) for the module of the conductivity tensor \mathbb{C} and the pressure p , as functions of time, together with the condition number of the matrix \mathcal{L} , for different values of r . We show for which values of the parameters we lose the symmetry of the two solutions.

4 Numerical Results

The numerical results focus on the effect of the regularization parameter r in (1), and how some properties of the numerical scheme are strictly connected to it.

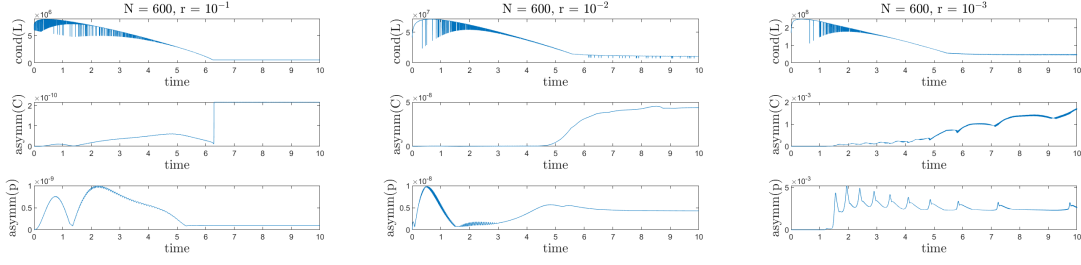


Figure 1: *Quantity defined in Eqs. (12-16) for the module of the conductivity tensor \mathbb{C} and the pressure p , as function of time, together with the condition number of \mathcal{L} , for different values of $r = 10^{-1}, 10^{-2}, 10^{-3}$.*

In our simulations we define the following initial conditions and source function S , as in equations (4) and (5):

$$C^{(1,1)}(t=0) = 1, \quad C^{(1,2)}(t=0) = 0 \quad C^{(2,2)}(t=0) = C^{(1,1)} \quad (12)$$

$$C^{(1,1)}(t=0) = (2 - |x + y|) \exp(-10|x - y|), \quad C^{(1,2)}(t=0) = 0, \quad C^{(2,2)}(t=0) = C^{(1,1)} \quad (13)$$

$$C^{(1,1)}(t=0) = 0, \quad C^{(1,2)}(t=0) = 0 \quad C^{(2,2)}(t=0) = C^{(1,1)} \quad (14)$$

$$S(\vec{x}) = E - \bar{E}, \quad E = \exp(-\sigma(\vec{x} - \vec{x}_0)^2), \quad \sigma = 500, \quad \vec{x}_0 = (0.25, 0.25) \quad (15)$$

where $\bar{E} = \text{mean}(E)$. The values of parameters of the system that we used in the simulations are as follows:

$$\alpha = 0.75, \quad c = 5, \quad D = 10^{-2}, \quad \varepsilon = 10^{-3}, \quad (16)$$

with number of points $N = 600$, time step $\Delta t = \Delta x$ and final time $t_{\text{fin}} = 10$. The choice of the parameter ε is justified in the recent paper [18], where we show that the solutions are qualitatively very close for $\varepsilon = 10^{-3}$ and $\varepsilon = 10^{-4}$.

In Fig. 1 we show how the symmetry of the the solutions strongly depends on the parameter r . We calculate the asymmetry of the two variables conductivity \mathbb{C} and pressure p , defined in Eq. (11), at each time step, and we compare these quantities with the conditioning number of the elliptic operator for the Poisson equation \mathcal{L} . Since the Eq. (1) is strongly degenerate for $r \rightarrow 0$, it is not possible to consider negligible values for the parameter.

To better understand how strong is the dependency, in Figs. 2-3 we show the plots of three different features of the solutions, the module at final time (a), the flux at final time (b) and the eigenvector associated to the greatest eigenvalue in absolute value (c), for $r = 10^{-2}, 10^{-3}, 10^{-4}$. We observe that the symmetry of the solution breaks for $r = 10^{-4}$, as we expected from Fig. 1, in which $\text{asymm}(\mathbb{C}) \approx 10^{-1}$.

In Fig. 4 we show the comparison between the solutions obtained with two different initial conditions, and choosing $r = 10^{-3}$: Eq. (12) for plots (a) and (c), and Eq. (14) for (b) and (d). Another difference among the plots is the diffusivity. We choose $D = 10^{-2}$ for plots (a) and (b), and $D = 0$ for plots (c) and (d). The main difference between (a) and (b) panels is the number of branches. Choosing zero initial condition, we see more branches respect to the one with initial condition constant, equal to one. This is an effect of the permeability tensor field $\mathbb{P}[\mathbb{C}] = \mathbb{C} + r\mathbb{I}$ in the elliptic operator. In panel (a), it is true that $\mathbb{C} > r = 10^{-3}$ at initial times, thus, even if we decrease r , the \mathbb{C} component is the one prevailing. On the contrary, in panel (b), choosing the initial condition equal to 0, it is r the parameter that is leading the elliptic operator at initial times, and being smaller than the module of the other initial condition, we are able to see more features. Regarding the case of zero diffusivity, we calculated the condition number of the elliptic operators, for the (c) panel $\text{cond}(L) = 7.030 \times 10^7$ and for the (d) panel $\text{cond}(L) = 9.845 \times 10^7$. This means that, with zero diffusivity, the stiffness of the system increases, and the solutions are less symmetric and accurate.

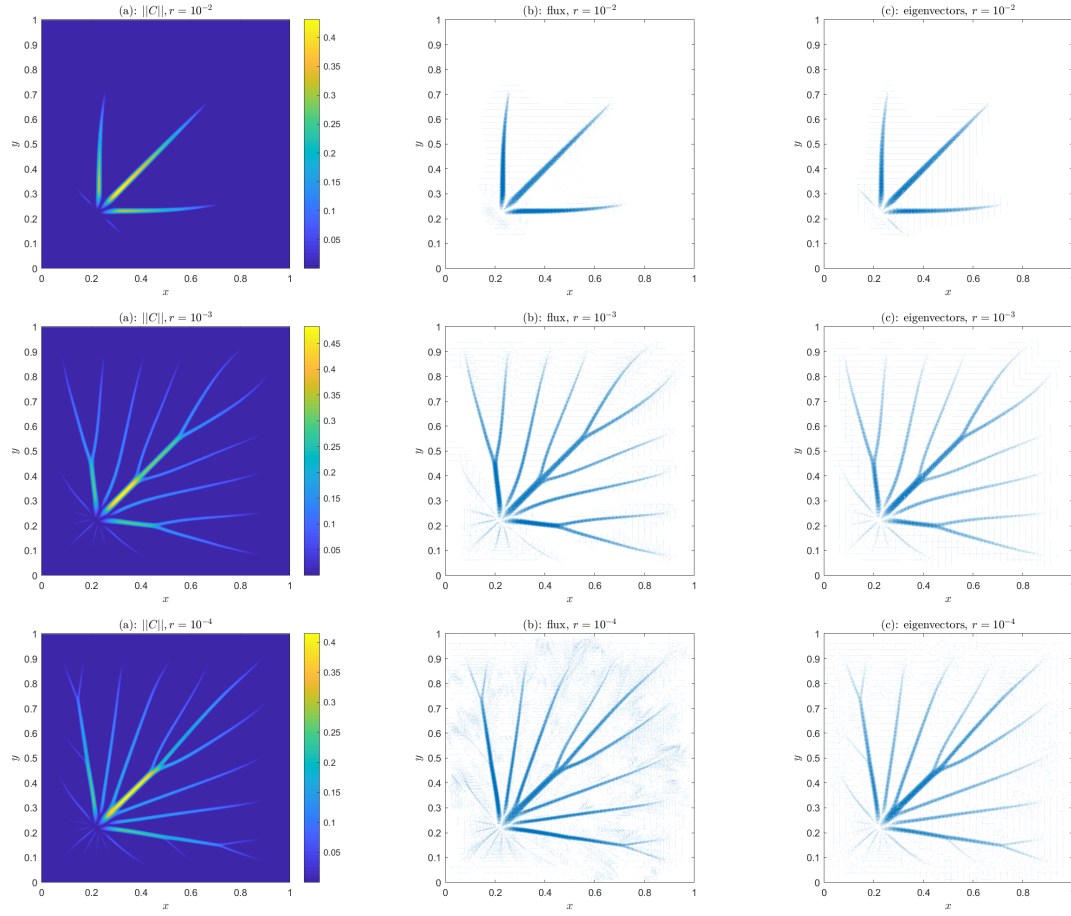


Figure 2: In this figure we show three different quantities of the same computations, with the parameters defined in Eq. (12): the module of the variables at final time (a), the flux at final time (b) and the eigenvectors associated to the greatest eigenvalue in absolute value (c). The first row is for $r = 10^{-2}$, the second row for $r = 10^{-3}$ and the last one for $r = 10^{-4}$. The rest of the data are defined in Eqs. (12-16).

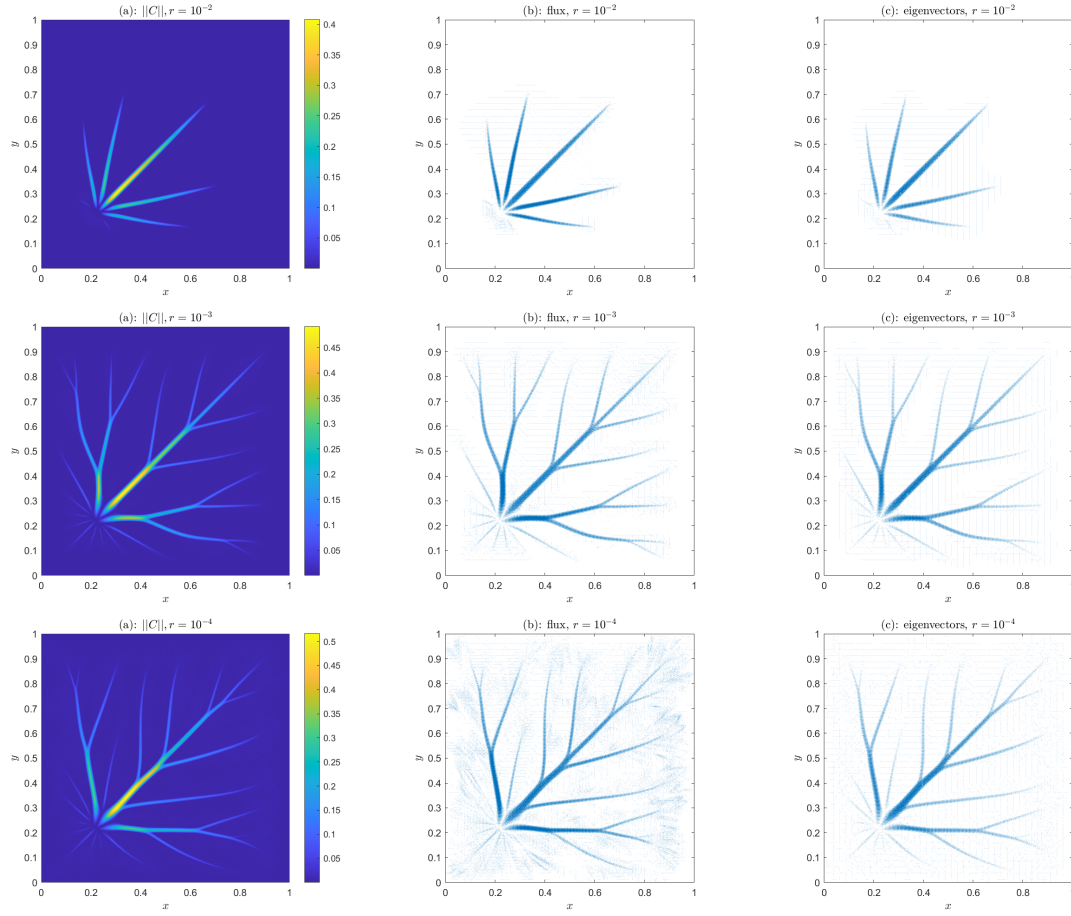


Figure 3: *In this figure we show three different quantities of the same computations, with the parameters defined in Eq. (13): the module of the variables at final time (a), the flux at final time (b) and the eigenvectors associated to the greatest eigenvalue in absolute value (c). The first row is for $r = 10^{-2}$, the second row for $r = 10^{-3}$ and the last one for $r = 10^{-4}$. The rest of the data are defined in Eqs. (12-16).*

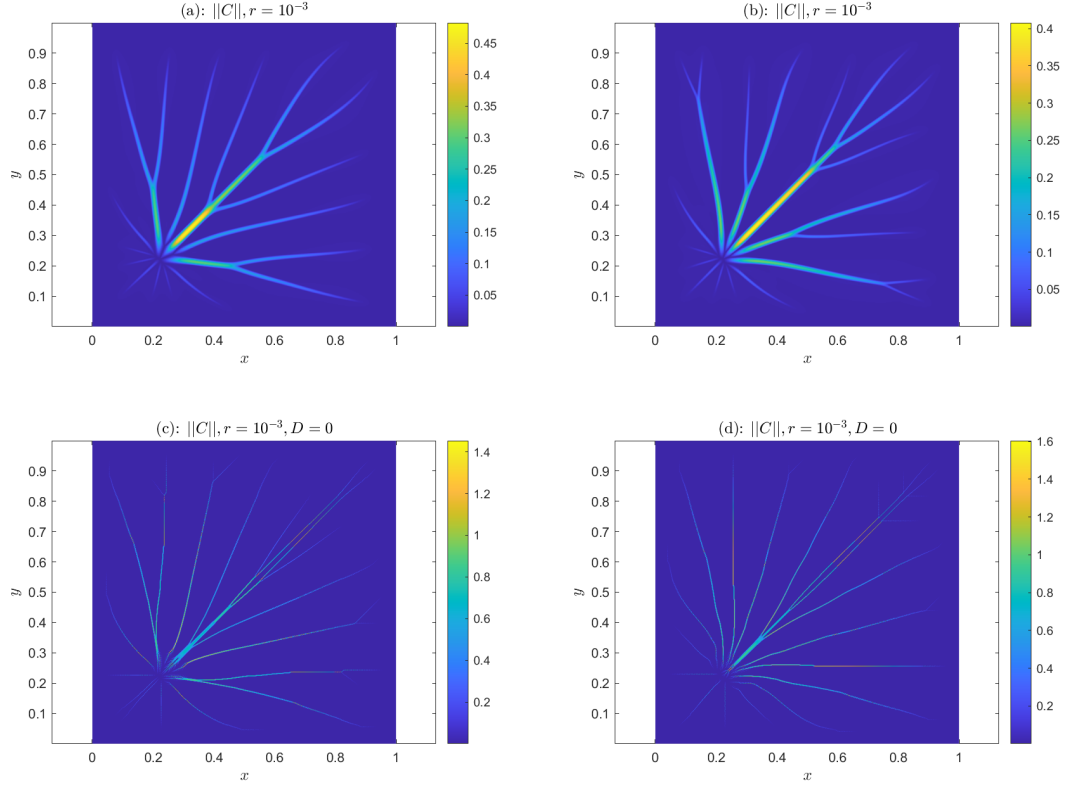


Figure 4: Comparison between the module of the solutions, at final time, with different initial conditions and diffusion coefficients D . In (a) and (c) the initial condition is defined in Eq. (12), while in (b) and (d) we have zero initial condition defined in Eq. (14). In plots (a) and (b) the diffusion coefficient is $D = 10^{-1}$, while in plots (c) and (d) we have zero diffusivity, i.e., $D = 0$.

4.1 Accuracy tests: Wasserstein distance

One possible way of introducing distance in function or measure spaces is the *Wasserstein distance*. This metric comes from the idea of moving a distribution of mass, minimizing the average of displacement, see Fig. 5 and, e.g., [23, 24, 25].

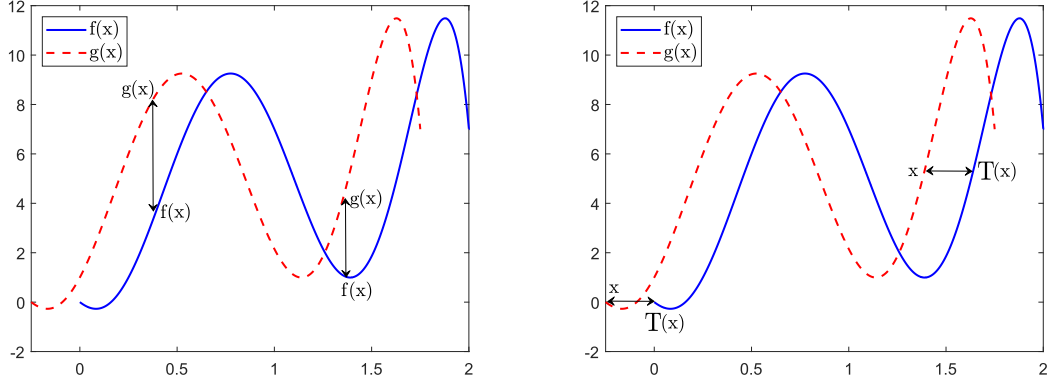


Figure 5: ‘Vertical’ vs ‘horizontal’ distances between a pair of functions. The figure demonstrates that, loosely speaking, Wasserstein distance depends more on the displacement of the function than its shape [26].

The Wasserstein distance of order $p \in [1, +\infty)$ between the probability measures μ, ν from the metric space (X, d) is defined as

$$W_p(\mu, \nu) = \left(\inf_{\pi \in \Pi(\mu, \nu)} \int_{X \times X} d(x, y)^p d\pi(x, y) \right)^{1/p}, \quad (17)$$

where $\Pi(\mu, \nu)$ is the set of all transference plans between μ and ν , i.e., measures on the product space $(X, d)^2$ with marginals μ and ν , respectively.

In Fig. 6 and Table 2 we give a comparison between the accuracy of our numerical simulations calculated with L^2 -norm and the Wasserstein metric¹ for $r = 10^{-2}$, on the left panel, and $r = 10^{-3}$, on the right panel. We used the initial datum (12) and the parameter settings specified in (12)–(16). We observe an improvement of the order of accuracy using the Wasserstein metric. When considering the L^2 norm, the error analysis does not seem to be affected by the number of points used in the space discretization.

¹<https://github.com/nklb/wasserstein-distance>

Table 2: Accuracy tests with Wasserstein distance, $\text{error}_{\mathcal{W}}$, and Richardson extrapolation, $\text{error}_{\mathcal{R}}$, for two different values of r : on the left $r = 10^{-2}$ and on the right $r = 10^{-3}$, at final time $t = 3$. With the Wasserstein distance, we are able to show the second order of the scheme, obtaining a result that is drastically better than the ones obtained with the usual norms. Here, again, we see that for a smaller values of r (right panel), the accuracy of the method gets worse. The rest of the data are defined in Eqs. (12-16).

| N | $\text{error}_{\mathcal{W}}$ | $\text{error}_{\mathcal{R}}$ |
|-----|------------------------------|------------------------------|
| 100 | - | - |
| 200 | 3.846e-03 | 3.358e-01 |
| 400 | 9.579e-04 | 2.763e-01 |
| 800 | 1.8060e-04 | 2.199e-01 |

| N | $\text{error}_{\mathcal{W}}$ | $\text{error}_{\mathcal{R}}$ |
|-----|------------------------------|------------------------------|
| 100 | - | - |
| 200 | 4.827e-03 | 3.273e-02 |
| 400 | 1.514e-03 | 3.292e-02 |
| 800 | 4.455e-04 | 2.609e-02 |

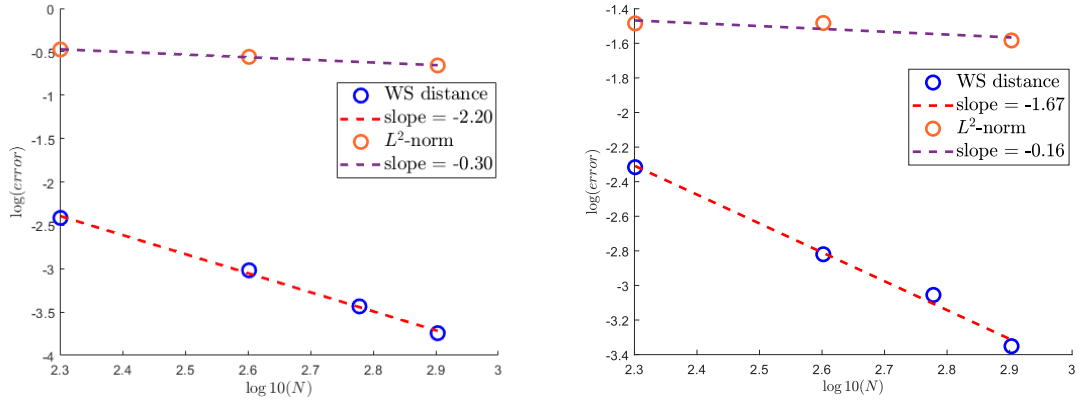


Figure 6: Comparison between the accuracy calculated with L^2 -norm and Wasserstein distance with initial condition defined in Eq. (12), with $r = 10^{-2}$ (left panel, without extrapolation technique in time) and $r = 10^{-3}$ (right panel, with extrapolation in time). The rest of the data are defined in Eqs. (12)–(16).

In Table 2 we present in the first column, the Wasserstein distance, $\text{error}_{\mathcal{W}}$, between one solution with N and $N/2$ number of grid points. In the second column we calculate the error with the Richardson extrapolation technique, $\text{error}_{\mathcal{R}}$. We observe an better rate of convergence when using the Wasserstein distance, which is related to the fact that the Wasserstein distance depends to a larger extent on the relative displacement of its arguments, i.e., the topological features of the network, rather than on the local values of the solution at each grid point.

5 Conclusions

In this paper we explored the effects of the background permeability parameter r in the elliptic-parabolic model (1)–(2) which represents a PDE framework describing the formation of biological networks. We showed that r is the parameter that influences the condition number of the elliptic operator in (1). When the condition number becomes too large, the symmetry of the numerical solution breaks down. As all the parameters of the system, the initial datum and the source function are symmetric, using a symmetric numerical scheme, we expect the solution to be symmetric at each time step. We make use of finite differences scheme to compute the solution of the system, with central differences for the space discretization and a *symmetric*-ADI method in time. Because of the non linearity in the Poisson equation, we make use of a time extrapolation to improve the accuracy convergence.

Moreover, we demonstrate that using the Wasserstein distance to measure the order of convergence of the numerical scheme provides better results than the L^2 norm, in particular when considering small values of the background permeability r . In [18] we were able to show the (expected) second order accuracy only in the case of $r = 0.1$. Here, using the Wasserstein distance to measure the error, we see a significant improvement even for much smaller values of the background permeability, $r = 10^{-2}$ and $r = 10^{-3}$.

In a future work we shall improve the numerical method by implementing a monolithic algorithm to solve the system. In that way, the two unknowns, conductivity tensor \mathbb{C} and pressure p , are solved implicitly at each time step, with the metabolic term that can be easily linearized. An application of IMEX schemes will ensure a higher order of accuracy. The monolithic scheme would also improve the stability in time, allowing us to consider larger time steps.

References

- [1] Robert Malinowski. Understanding of leaf development – the science of complexity. *Plants*, 2(3):396–415, 2013.
- [2] David Sedmera. Function and form in the developing cardiovascular system. *Cardio-vascular research*, 91(2):252–259, 2011.
- [3] Anne Eichmann, Ferdinand Le Noble, Monica Autiero, and Peter Carmeliet. Guidance of vascular and neural network formation. *Current opinion in neurobiology*, 15(1):108–115, 2005.
- [4] Olivier Michel and Joëlle Biondi. Morphogenesis of neural networks. *Neural Processing Letters*, 2(1):9–12, 1995.

- [5] Ulrich Pohl, Jurgen Holtz, Rudi Busse, and Eberhard Bassenge. Crucial role of endothelium in the vasodilator response to increased flow in vivo. *Hypertension*, 8(1):37–44, 1986.
- [6] WJ Hacking, E VanBavel, and JA Spaan. Shear stress is not sufficient to control growth of vascular networks: a model study. *American Journal of Physiology-Heart and Circulatory Physiology*, 270(1):H364–H375, 1996.
- [7] AR Pries, TW Secomb, and P Gaehtgens. Structural adaptation and stability of microvascular networks: theory and simulations. *American Journal of Physiology-Heart and Circulatory Physiology*, 275(2):H349–H360, 1998.
- [8] Qi Chen, Luan Jiang, Chun Li, Dan Hu, Ji-wen Bu, David Cai, and Jiu-lin Du. Haemodynamics-driven developmental pruning of brain vasculature in zebrafish. 2012.
- [9] Dan Hu, David Cai, and Aaditya V Rangan. Blood vessel adaptation with fluctuations in capillary flow distribution. 2012.
- [10] Dan Hu and David Cai. Adaptation and optimization of biological transport networks. *Physical review letters*, 111(13):138701, 2013.
- [11] Dan Hu. Optimization, adaptation, and initialization of biological transport networks. *Notes from lecture*, 1:3–1, 2013.
- [12] Jan Haskovec, Peter Markowich, and Benoit Perthame. Mathematical analysis of a pde system for biological network formation. *Communications in Partial Differential Equations*, 40(5):918–956, 2015.
- [13] Jan Haskovec, Peter Markowich, Benoît Perthame, and Matthias Schlottbom. Notes on a pde system for biological network formation. *Nonlinear Analysis*, 138:127–155, 2016. Nonlinear Partial Differential Equations, in honor of Juan Luis Vázquez for his 70th birthday.
- [14] Giacomo Albi, Marco Artina, Massimo Foransier, and Peter A. Markowich. Biological transportation networks: Modeling and simulation. *Analysis and Applications*, 14(01):185–206, 2016.
- [15] Giacomo Albi, Martin Burger, Jan Haskovec, Peter Markowich, and Matthias Schlottbom. *Continuum Modelling of Biological Network Formation*. Modelling and Simulation in Science and Technology. Birkhäuser-Springer (Boston), 2017.
- [16] Jan Haskovec, Peter A. Markowich, and Simone Portaro. Emergence of biological transportation networks as a self-regulated process, 2022.
- [17] Jan Haskovec, Peter Markowich, and Giulia Pilli. Tensor pde model of biological network formation. *Communications in Mathematical Sciences*, 20(4):1173–1191, 2022.

- [18] Clarissa Astuto, Daniele Boffi, Jan Haskovec, Peter Markowich, and Giovanni Russo. Comparison of two aspects of a pde model for biological network formation. *Mathematical and Computational Applications*, 27(5), 2022.
- [19] J.A. Carrillo and G. Toscani. *Wasserstein metric and large-time asymptotics of nonlinear diffusion equations*, pages 234–244.
- [20] Felix Otto. *Double degenerate diffusion equations as steepest descent*. Citeseer, 1996.
- [21] Felix Otto. The geometry of dissipative evolution equations: the porous medium equation. *Communications in Partial Differential Equations*, 26(1-2):101–174, 2001.
- [22] Antonio Raudino, Antonio Grassi, Giuseppe Lombardo, Giovanni Russo, Clarissa Astuto, and Mario Corti. Anomalous sorption kinetics of self-interacting particles by a spherical trap. *Communications in Computational Physics*, 31(3):707–738, 2022.
- [23] Cedric Villani. Topics in optimal transportation.(books). *OR/MS Today*, 30(3):66–67, 2003.
- [24] Cédric Villani. *Optimal transport: old and new*, volume 338. Springer, 2009.
- [25] Luigi Ambrosio, Nicola Gigli, and Giuseppe Savaré. *Gradient flows: in metric spaces and in the space of probability measures*. Springer Science & Business Media, 2005.
- [26] Filippo Santambrogio. {Euclidean, metric, and Wasserstein} gradient flows: an overview. *Bulletin of Mathematical Sciences*, 7(1):87–154, 2017.